Detailed modeling of hydrocarbon nanoparticle nucleation in acetylene discharges

Kathleen De Bleecker* and Annemie Bogaerts
PLASMANT, Department of Chemistry, University of Antwerp, Universiteitsplein 1, 2610 Wilrijk, Belgium

Wim Goedheer
FOM—Institute for Plasma Physics "Rijnhuizen," Association EURATOM-FOM, Trilateral Euregio Cluster, P. O. Box 1207, 3430 BE Nieuwegein, The Netherlands

(Received 16 November 2005; published 22 February 2006)

The initial stage of nanoparticle formation and growth in radiofrequency acetylene (C_2H_2) plasmas is investigated by means of a self-consistent one-dimensional fluid model. A detailed chemical kinetic scheme, containing electron impact, ion-neutral, and neutral-neutral reactions, has been developed in order to predict the underlying dust growth mechanisms and the most important dust precursors. The model considers 41 different species (neutrals, radicals, ions, and electrons) describing hydrocarbons (C_nH_m) containing up to 12 carbon atoms. Possible routes for particle growth are discussed. Both positive and negative ion reaction pathways are considered, as consecutive anion- and cation-molecule reactions seem to lead to a fast build up of the carbon skeleton.

DOI: 10.1103/PhysRevE.73.026405 PACS number(s): 52.27.Lw, 52.65.−y, 82.33.Xj, 52.80.Pi

I. INTRODUCTION

Thin films of hydrogenated amorphous carbon (a-C:H) are routinely deposited by the plasma enhanced chemical vapor deposition (PECVD) technique by decomposition of hydrocarbon gases such as methane or acetylene. These carbon-based coatings with extraordinary material properties (i.e., a combination of high hardness, chemical inertness, low abrasive coefficient, and infrared transparency) are of great interest for a myriad of industrial applications, including tribological materials [1,2], passivation layers [3], and field emission cold cathodes for future flat-screen displays [4–6]. Deposition at low pressure and high power generally leads to the fabrication of so-called diamondlike carbon layers, which are frequently used as antiwear coatings for machine tools, and as hard protective coatings on computer hard disk drives, optical windows, and microelectromechanical devices [3,7–9].

Even though the PECVD technique has the ability of creating uniform thin films on a wide variety of substrates, it can have the disadvantage of generating nano- or micrometer-sized particles, causing the creation of dusty plasmas or complex plasma systems. The nucleation of these nanoparticles in the gas phase usually limits the growth rate of the film and equipment utilization, as the incorporated dust particles can cause film delamination, structural voids, and dislocations that ultimately lead to malfunctioning devices. The problem is especially acute in the microelectronics industry, where dust is considered as a leading source of yield loss in the processing devices. During a number of years the main research goal of plasma processing reactors was to control this contamination, either by removal of the formed dust particles from the ionized gas phase or by preventing contact with the processing area. Recently, however, it was found that nanoparticles can also play a positive role in certain material science applications. Efficient electron emission has, for example, been observed from amorphous carbon thin films composed of nanoparticles [10,11], making them a promising material for the fabrication of field electron emitters. Due to their large surface to volume ratio, the layers are also introduced in the catalytic and electromechanical industry for the construction of nanoscale materials [3,10].

In order to control the nanoparticle growth and physical properties in all the above-mentioned and future technological applications, a fundamental understanding of the particle formation mechanisms and dynamics is indispensable. Comprehension of these aspects can help in finding efficient ways to either eliminate "killer" particles or enhance structural incorporation of nanoparticles under the control of their size and morphology. Although in the silicon industry widespread research has dealt with the reaction kinetics and nanoparticle formation chemistry of silane plasmas [12–15], very little attention has so far been paid to hydrocarbon dusty plasmas and hence the conditions for carbonaceous dust formation are not well understood.

In the present study acetylene (C_2H_2) is considered as an example of the hydrocarbon discharge chemistry, as it yields more highly polymerized ions than methane (CH_4) and also has a much stronger and faster tendency to produce dust [16]. Other hydrocarbon gas mixtures also tend to produce dust, particularly when a sufficient amount of acetylene is present [17]. It is generally assumed that in chemically active plasmas, such as acetylene, particles emerge as a result of numerous consecutive chemical reactions in the ionized gas phase, known as gas phase polymerization [17]. So far a few experimental and theoretical studies on the chemical kinetics of acetylene discharges have been made. Doyle [18] proposed a simple reaction mechanism that accounts for the production of C_4H_2 and C_6H_2 species and the film deposition rate. Attention was mainly focused on the neutral chemistry and it was assumed that ions play a minor role in the overall

*Electronic address: kathleen.debleecker@ua.ac.be

plasma chemistry. Appropriate estimations for several rate constants are made based on the experimentally measured partial pressures of the product gases H_2, C_4H_2, and C_6H_2. It was concluded that the film growth is mainly dominated by the radicals C_4H_3, C_6H_3, and C_2H. Herrebout *et al.* [19] developed a one-dimensional (1D) fluid model that describes the base reaction mechanism of small species in a typical rf acetylene discharge, but did not include any dust growth. Consequently, no electron attachment to acetylene and, hence, no negative ions that can undergo ion-neutral reactions leading to the formation of larger particles have been taken into account in the model. Deschenaux *et al.* [16] presented a comprehensive mass spectrometry study of a dusty rf acetylene plasma. The positive and negative ion mass spectra clearly showed the formation of higher-mass hydrocarbon cations and anions up to nearly 200 amu corresponding to species containing 14–15 carbon atoms. Their results indicated the existence of several pathways that may lead to effective particle production. Stoykov *et al.* [20] recently developed a zero-dimensional chemical kinetic clustering model that considers the growth of linear chain and cyclic hydrocarbon molecules containing up to ten carbon atoms. Although the model contains a diverse number of chemical reactions (including electron attachment, neutralization, and even diffusion losses to the discharge walls), Stoykov *et al.* did not investigate the role of positively charged hydrocarbon clusters and even assumed a constant $C_4H_2^+$ positive ion concentration in order to provide for a constant degree of ionization. The observation of higher-mass hydrocarbon cations in the positive ion mass spectrum seems, however, to warrant their explicit consideration as a possible route of powder formation. Furthermore, a primary ionic reaction sequence starting from $C_2H_2^+$ has already been defined from the mass spectrometry measurements of Vasile and Smolinsky [21].

Hence, even for simple monomers like acetylene the generation of hydrocarbon nanoparticles seems to be a very complex process that is mediated by a large number of elementary reactions in the ionized gas phase. The objective of this paper is to provide an extensive investigation of the initial stage of nanoparticle generation, i.e., particle nucleation, in a capacitively coupled acetylene rf discharge by means of a self-consistent one-dimensional fluid model. In order to obtain more insight into the complexity of the carbonaceous plasma a detailed chemical kinetic scheme has been developed. In our model the electron kinetics and the plasma chemistry as well as the deposition process are described in a fully self-consistent way, and the model thus inherently also incorporates a coupling between the growth of the particles and the changes they induce in the plasma properties. Furthermore, by solving the electron energy distribution function (EEDF) using the Boltzmann equation in a two-term approximation we are able to obtain the electron collision rates and the electron transport coefficients as a function of the average electron energy. Hence, in contrast to the numerical model of Stoykov *et al.* [20] we do not assume a Maxwellian distribution, as the EEDF can often deviate significantly and is influenced by the composition of the background gas [22]. A similar fluid model has recently also been developed to investigate the initial cluster formation mechanisms of hydrogenated silicon particles in pure silane discharges [15,23]. The dust formation pathway is in that case mainly dominated by anion-induced chain reactions which are mostly triggered by the SiH_3^- anion [15].

In the present model the most important mechanism of carbonaceous dust formation is by the stepwise integration of consecutive ion-molecule reactions that lead to the formation of larger hydrocarbon species. Since particle nucleation is at this point our main interest, hydrocarbons containing up to a maximum of 12 carbon atoms have been included. Presumably both positive and negative ions play a role in the initial phase of particle formation, as the mass spectrometry measurements reveal the same features in both the anion and cation mass spectra. Due to the lack of exact data on several processes in the acetylene discharge some approximations had to be made, which were validated against the information obtained from the experimental mass spectra of Deschenaux *et al.* [16]. Additional information could also be collected from the reaction mechanisms that are used to predict the nucleation of soot particles during combustion in hydrocarbon flames and arcs [24,25]. Carbonaceous dust plays additionally a role in astrophysics as the precursor for planet and carbon-rich circumstellar envelope formation [26].

Further chain propagation will eventually lead to the formation of nano- and micrometer-sized particles that will quickly acquire a negative charge due to the collection of plasma ions and electrons and are confined to some well-defined regions of the plasma by the dynamic balance of the ion drag and thermophoretic and other existent forces [27,28]. In the end gravity pulls the particles out of the discharge.

The structure of the paper is as follows. An overview of the model is given in Sec. II, including a detailed description of all the relevant particle growth mechanisms that are introduced in the chemical kinetic scheme. The numerical results are discussed in Sec. III. Besides a description of the particle density profiles, theoretically predicted mass spectra have been deduced from the fluxes of the different positive and negative ions toward the discharge walls and are compared with the experimental data. The effect of hydrogen dilution on the propensity of higher-polymerized-ion formation is also studied. Finally, the conclusions are given in Sec. IV.

II. MODEL DESCRIPTION

A capacitively coupled radio-frequency discharge (13.56 MHz) in a parallel plate reactor is simulated. Due to the large number of species and reactions treated in the plasma module a fluid modeling approach is warranted in order to accurately describe the first stage of particle formation in a reactive acetylene plasma. No particle-in-cell Monte Carlo method is required, since we do not reach very low pressures where the mean free path becomes comparable to the gap between the electrodes [29]. First, a general overview of the fluid model is provided, followed by a comprehensive description of the different species and the particle generation mechanisms.

A. Mass, flux, and energy balance equations

In a 1D fluid model particle, momentum and energy density balance equations are derived from the velocity moments of the Boltzmann equation. The Poisson equation, needed to calculate the electric field, is coupled to the balance equations, making the model fully self-consistent. Typical calculation results include the density profiles and fluxes of the different species, as well as discharge quantities such as the electric field and potential, all as functions of space and time. For every plasma species (electrons, ions, radicals, and molecules) a density balance equation is constructed that takes into account all different production and loss mechanisms:

$$\frac{dn_j}{dt} + \frac{d\Gamma_j}{dx} = S_j \tag{1}$$

where n_j, and Γ_j are the particle's density and flux, respectively, and S_j describes the different source and sink terms of particle j, i.e., formation and destruction. The gas inlet and pumping are also incorporated by means of additional source and sink terms.

In the model the momentum conservation equation is replaced by a drift-diffusion approximation; hence, the transport equation is reduced to a diffusion term for the neutral species (radicals and molecules) and consists of two separate terms, i.e., a migration and a diffusive term, in the case of charged particles (ions and electrons):

$$\Gamma_j = \mu_j n_j E - D_j \frac{dn_j}{dx}. \tag{2}$$

μ_j and D_j are the mobility and diffusion coefficient of particle j, and E represents the electric field. Note that for the ions an effective electric field E_{eff} is considered that compensates the inertia effects originating from the ions' lower momentum transfer frequency.

An energy balance equation is incorporated for the electrons:

$$\frac{dn_e\epsilon}{dt} + \frac{d\Gamma_w}{dx} = -e\Gamma_e E + S_w, \tag{3}$$

which includes Ohmic heating and the loss of energy due to electron impact collisions, described by the first and second terms on the right-hand side, respectively. ϵ is the average electron energy and Γ_w represents the electron energy density flux:

$$\Gamma_w = \frac{5}{3}\mu_e n_e \epsilon E - \frac{5}{3} D_e \frac{dn_e\epsilon}{dx}. \tag{4}$$

The source terms of the electron impact collisions are obtained from the electron energy distribution function and are expressed as a function of the average electron energy ϵ. No energy balance equation is included for the ions and neutrals, as they are assumed to be in thermal equilibrium with the background gas.

Finally, the Poisson equation is needed to obtain the electric field E and the potential V self-consistently:

$$\frac{d^2V}{dx^2} = -\frac{e}{\epsilon_0}\left(\sum n_+ - \sum n_- - n_e\right), \quad E = -\frac{dV}{dx}, \tag{5}$$

where n_+, n_- and n_e denote the positive ion, negative ion, and electron density, respectively.

The system of nonlinear coupled differential equations is solved numerically on an equidistant mesh containing 64 different grid points. The spatial discretization of the balance equations is based on an implicit finite-difference technique using the Scharfetter-Gummel exponential scheme. Convergence of the fluid model is reached when the relative changes of the discharge parameters between two succeeding rf cycles are less than 10^{-6}. The time step within a rf cycle (13.56 MHz) is set to 9.2×10^{-10} s (i.e., the rf cycle is divided into 80 time steps). For further description of the applied discretization schemes and solution procedures we refer to [22].

B. Plasma chemical kinetics

The generation of nanometer-sized particles in reactive acetylene plasmas is a very complex process that is mediated by a large amount of chemical reactions in the ionized gas phase. First, small species (e.g., radicals, ions, atoms, and molecules) are generated by electron impact decomposition of the C_2H_2 feed gas. Larger clusters can then be formed as a result of consecutive polymerization reactions, which are triggered by certain reactive precursors. In order to describe this nucleation process, a detailed chemical kinetic scheme has been developed. In our model we account for 92 volume reactions involving 20 neutral and 21 charged species and consider hydrocarbons containing up to a maximum of 12 carbon atoms. Since exact data on the molecular level of the C_2H_2 discharge chemistry are sometimes lacking, a few approximations had to be made. These applied assumptions, and thus also the model, are validated by comparing our acquired results with the experimentally obtained mass spectra shown in Fig. 1, reproduced from Deschenaux *et al.* [16] (see below for a detailed discussion). In the following paragraphs a comprehensive description is given of the most important species and all the relevant reaction mechanisms.

1. Species included in the model

Table I provides an overview of the 40 different species considered in the plasma module, besides the electrons. The type of species included in the model is based on experimental observations, like the mass spectra illustrated in Fig. 1. The absence of hydrocarbon molecules with an odd number of carbon atoms is a distinct feature of acetylene discharges. The typical spectral pattern in Fig. 1 shows the clear dominance of species with an even number of carbon atoms indicating that the strong carbon triple bond of the initial acetylene molecule (H—C≡C—H) persists upon consecutive integration of acetylene in larger building units. Therefore, mostly carbon species with an even number of carbon atoms have been incorporated.

The largest species considered in our model include twelve carbon atoms. C_2H_2 and H_2 are the main neutral molecules. Although their vibrationally excited levels are not

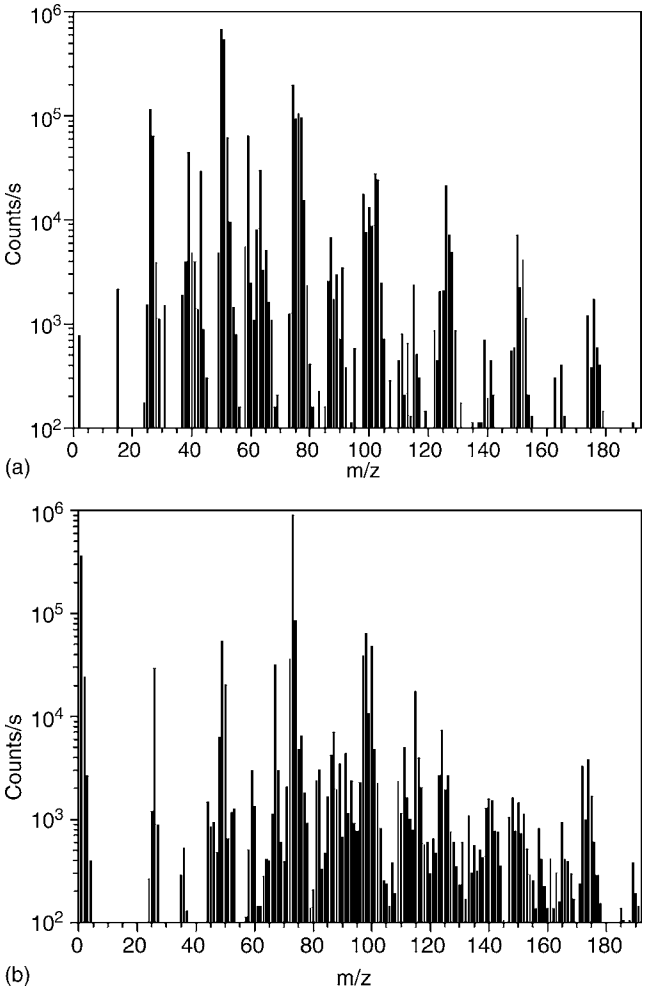

FIG. 1. Mass spectra of the (a) positive ions and (b) negative ions in an acetylene discharge. Reproduced with permission from [16].

represented by separate species in our model, the major energy loss due to electron impact vibrational excitation is taken into account (see Table II). In order to reduce the computational effort, we simply treat the vibrationally excited states as ground state molecules, thus not requiring a separate calculation of their concentration. Higher-order hydrocarbon molecules ($C_{2n}H_2$), such as diacetylene, are also present at relatively high densities and thus cannot be excluded. Mainly carbon-rich species C_mH_n with $m>n$ have been inserted, since a low hydrogen content is typically observed in many of the generated hydrocarbon species in the acetylene discharge [16,36]. For the ions both positive and negative ions up to 12 carbon atoms are considered, as they presumably both play a role in the initial stage of particle generation. Since the role and presence of aromatic compounds in the carbonaceous dust production of low-temperature acetylene plasmas is still unclear, no cyclic rings have been included in the present chemical kinetic scheme (for further explanation see Sec. II B 8).

2. Electron collisions

Acetylene molecules can be excited, dissociated, or ionized through various electron impact collisional processes resulting in the formation of radicals, ions, and atoms. Calculation of the rate constants of these electron-induced reactions requires the knowledge of the electron energy distribution function, as well as the energy-dependent cross sections. By solution of the EEDF from the two-term expansion of the Boltzmann equation and the known cross sections, we can obtain the electron collision rates as a function of the average electron energy. Figure 2 shows the various cross sections for electron impact on C_2H_2 and H_2 used to calculate the rates of the electron reactions presented in Table II. The number on each curve refers to the reaction number specified in Table II. For a better visualization of their profile, the electron impact ionization cross sections are plotted on a larger energy scale in Fig. 2(b), while cross sections that exhibit a lower energy threshold (i.e., dissociation, vibrational excitation, and dissociative attachment) are shown in Fig. 2(a). The threshold energies and references of the 23 electron-neutral reactions are outlined in Table II.

a. Ionization. Acetylene is unique in that it does not readily lose hydrogen atoms or hydrogen molecules on electron impact ionization, which manifests itself in cross sections that exhibit a relatively high energy threshold for dissociative ionization processes. Electron impact ionization of C_2H_2 produces $C_2H_2^+$, whereas dissociative ionization can produce C_2H^+, C_2^+, CH^+, C^+, and H^+. Partial cross sections for the various ionic fragment channels have been accurately measured (uncertainty $\leqslant 10\%$) by Tian and Vidal [37] in the electron impact energy range varying from threshold to 600 eV. Janev and Reiter [30] extended these data to higher energies, i.e., beyond 1000 eV, and have fitted both the total and partial ionization cross sections to one appropriate analytic expression,

TABLE I. Different species considered in the acetylene chemistry model, besides the electrons.

Molecules	Ions	Radicals
C_2H_2	$C_2H_2^+$, C_2H^+, CH^+, C_2^+, C^+	CH, CH_2
		C_2H_3, C_4H_3, C_6H_3
C_4H_2, C_6H_2, C_8H_2	$C_4H_2^+$,$C_6H_2^+$, $C_6H_4^+$, $C_8H_4^+$	
$C_{10}H_2$, $C_{12}H_2$	$C_8H_6^+$, $C_{10}H_6^+$, $C_{12}H_6^+$	$C_{12}H_6$
H_2	H_2^+, H^+	H
	C_2H^-, C_4H^-, C_6H^-	C_2H, C_4H, C_6H
	C_8H^-, $C_{10}H^-$, $C_{12}H^-$	C_8H, $C_{10}H$, $C_{12}H$

TABLE II. The electron impact collisions and their corresponding threshold energies considered in the 1D fluid model. The abbreviation "est." stands for estimated.

	Reaction	Threshold energy (eV)	Reaction type	Reference
1.	$C_2H_2+e^-\rightarrow C_2H_2^++2e^-$	11.4	Ionization	[30]
2.	$C_2H_2+e^-\rightarrow C_2H^++H+2e^-$	16.5	Dissociative ionization	[30]
3.	$C_2H_2+e^-\rightarrow C_2^++H_2+2e^-$	17.5	Dissociative ionization	[30]
4.	$C_2H_2+e^-\rightarrow CH^++CH+2e^-$	20.6	Dissociative ionization	[30]
5.	$C_2H_2+e^-\rightarrow C^++CH_2+2e^-$	20.3	Dissociative ionization	[30]
6.	$C_2H_2+e^-\rightarrow H^++C_2H+2e^-$	18.4	Dissociative ionization	[30]
7.	$C_2H_2^{(0)}+e^-\rightarrow C_2H_2^{(\nu=5)}+e^-$	0.09	Vibrational excitation	[31]
8.	$C_2H_2^{(0)}+e^-\rightarrow C_2H_2^{(\nu=2)}+e^-$	0.29	Vibrational excitation	[31]
9.	$C_2H_2^{(0)}+e^-\rightarrow C_2H_2^{(\nu=3)}+e^-$	0.41	Vibrational excitation	[31]
10.	$C_2H_2+e^-\rightarrow C_2H+H+e^-$	7.5	Dissociation	[30]
11.	$C_2H_2+e^-\rightarrow C_2H^-+H$	1.66	Dissociative attachment	[32]
12.	$H_2+e^-\rightarrow H_2^++2e^-$	15.4	Ionization	[33]
13.	$H_2+e^-\rightarrow H_2^{(\nu=1)}+e^-$	0.54	Vibrational excitation	[34]
14.	$H_2+e^-\rightarrow H_2^{(\nu=2)}+e^-$	1.08	Vibrational excitation	[34]
15.	$H_2+e^-\rightarrow H_2^{(\nu=3)}+e^-$	1.62	Vibrational excitation	[34]
16.	$H_2+e^-\rightarrow H+H+e^-$	8.9	Dissociation	[35]
17.	$C_4H_2+e^-\rightarrow C_4H+H+e^-$	7.5	Dissociation	[30], est.
18.	$C_6H_2+e^-\rightarrow C_6H+H+e^-$	7.5	Dissociation	[30], est.
19.	$C_8H_2+e^-\rightarrow C_8H+H+e^-$	7.5	Dissociation	[30], est.
20.	$C_{10}H_2+e^-\rightarrow C_{10}H+H+e^-$	7.5	Dissociation	[30], est.
21.	$C_{12}H_2+e^-\rightarrow C_{12}H+H+e^-$	7.5	Dissociation	[30], est.
22.	$C_4H_2+e^-\rightarrow C_4H_2^++2e^-$	11.4	Ionization	[30], est.
23.	$C_6H_2+e^-\rightarrow C_6H_2^++2e^-$	11.4	Ionization	[30], est.

$$\sigma_{ion}=\frac{10^{-17}}{EI_c}\left[A_1\ln\left(\frac{E}{I_c}\right)+\sum_{j=2}^{N}A_j\left(1-\frac{I_c}{E}\right)^{j-1}\right](m^2) \quad (6)$$

where I_c has a value equal or close to the appearance potential and E is the collision energy, both expressed in eV. A_j represent the different fitting parameters for each partial cross section. When the number of fitting parameters is set to six, a deviation with a rms no larger than 2–3% is attained [30]. For every electron impact ionization the parametric I_c and A_j values are given in Table XVIII of Ref. [30]. The ionization cross sections seem to be characterized by a relatively steep rise immediately after the threshold, a broad maximum in the energy region of 70–100 eV, and a drop beyond the maximum in the form of $E^{-1}\ln(E)$.

For the production of $C_4H_2^+$ and $C_6H_2^+$ from C_4H_2 and C_6H_2, respectively, the C_2H_2 electron impact ionization cross section has been used as an approximation, since no data concerning their cross sections are available in literature.

b. Dissociation. Electron-induced dissociation of C_2H_2 mainly forms the ethynyl radical C_2H by hydrogen abstraction. Unfortunately, to our knowledge the cross sections for neutral production from C_2H_2 have not been determined. The threshold for electron impact dissociation should, however, typically be several eV lower than the threshold for electron impact ionization. As an approximation the electron impact dissociative excitation (DE) of C_2H_2 to C_2H radicals has been adopted. An appropriate analytical expression for the C_2H production can be derived from the general expression for the total dissociative excitation cross section of C_2H_y molecules proposed by Janev and Reiter [30],

$$\sigma_{DE}^{tot}(C_2H_2)=34.6F_2^{DE}\left(1-\frac{E_{th}}{E}\right)^3\frac{1}{E}\times\ln(e+0.15E) \quad (10^{-20}\ m^2) \quad (7)$$

where F_2^{DE} is equal to 1.704 in the case of C_2H_2, E_{th}, and E are the threshold and the collision energies expressed in eV units, respectively, and e is the base of the natural logarithm. The cross section for the particular dissociative excitation channel

$$C_2H_2+e\rightarrow C_2H+H+e \quad (8)$$

can be obtained from the relation [30],

$$\sigma_{DE}(C_2H/C_2H_2)=\tilde{R}_{DE}(C_2H/C_2H_2)\sigma_{DE}^{tot} \quad (9)$$

where $\tilde{R}_{DE}(C_2H/C_2H_2)$ is the branching ratio for the C_2H DE channel, which depends on the energy of the impinging electron,

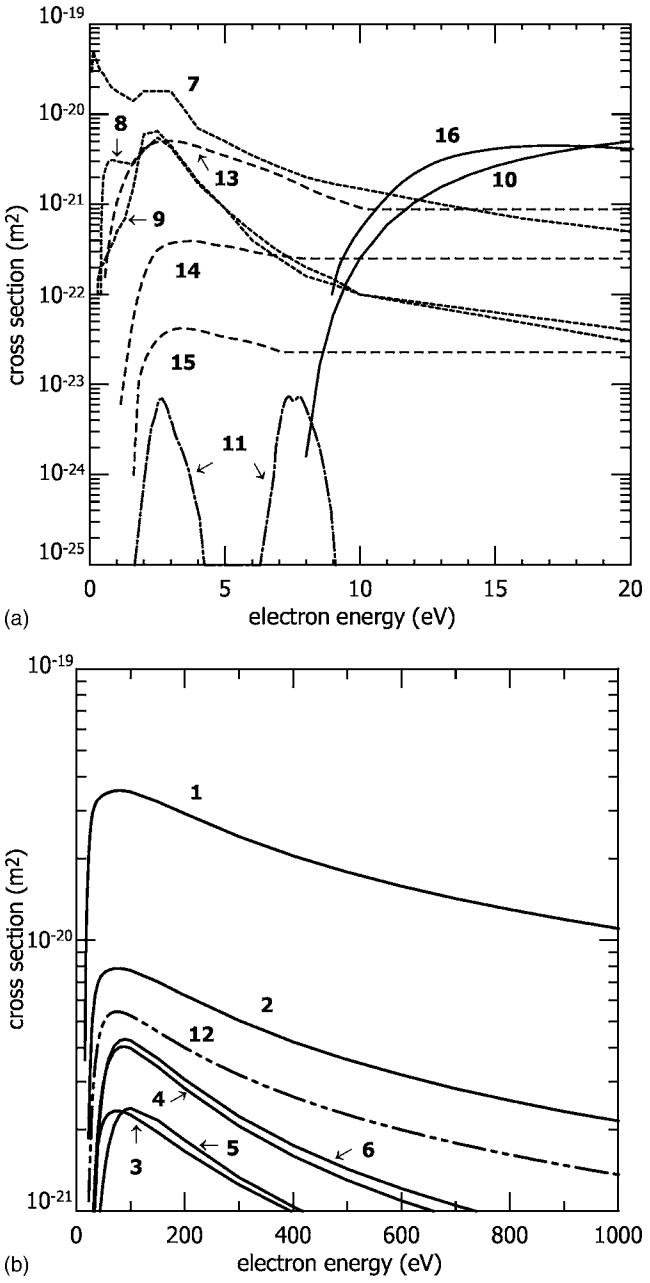

FIG. 2. Cross sections of the electron impact collisions of C_2H_2 and H_2: (a) vibrational excitation, dissociation, and dissociative attachment; (b) electron impact ionization. The number on each curve refers to the reaction number specified in Table II. Curves 1 and 10 have also been used as an approximation for the unknown cross sections of reactions 22,23 and 17–21, respectively (see text).

$$\tilde{R}_{DE}(E) = \frac{R'_{DE}}{1 - \chi(E_{th}/E)^{\beta}} \tag{10}$$

with $\chi = 1 - R'_{DE}$ and the parameter $\beta \cong 1.5$. The asymptotic value R'_{DE} for C_2H is equal to 0.51 [30].

The approach of using the electron dissociative excitation process for the calculation of the unknown dissociation cross section seems warranted when comparing our obtained reaction rate coefficient with other reported estimates. At the average electron energy of 3 eV we obtain a rate constant of 1.29×10^{-16} m^3 s^{-1}, which is very close to the value suggested in the theoretical and experimental work of Tibbitt *et al.*, i.e., 1.66×10^{-16} m^3 s^{-1} [38]. Stoykov *et al.* estimated a somewhat lower value of the order of 9.96×10^{-17} m^3 s^{-1}, which was derived from the electron dissociative ionization cross sections reduced by one order of magnitude [20].

Dissociation or hydrogen abstraction can also occur from higher-mass hydrocarbon molecules $C_{2n}H_2$ (with $n=2-6$) (see reactions 17–21 in Table II). Since the dissociation energy for a carbon-hydrogen bond fissure mainly depends on the chemical bond structure of the involved carbon atom, the C_2H_2 dissociation cross section can also be applied.

c. Vibrational excitation. Even though the vibrational modes are not regarded separately in the model, the vibrational excitation of the background C_2H_2 and H_2 molecules is considered in the Boltzmann equation for the proper calculation of the electron energy. For C_2H_2 the differential cross sections for the excitation of the ν_2 (symmetric C≡C stretching), the ν_3 (asymmetric stretching), and the ν_5 (asymmetric bending) vibrational modes have been measured in detail by Kochem *et al.* [39] for impact energies of the electrons from threshold to 3.6 eV. The cross sections show a shape resonance of $^2\Pi_g$ symmetry around 2.6 eV and are characterized by a steep threshold at the vibrational energies. The study of the vibrations ν_1, symmetric C—H bending, and ν_4, symmetric bending, is more limited because these Raman-active modes are not strongly excited in this energy region and thus overlap with the stronger infrared-active ν_3 and ν_5 modes, respectively, which prohibits their separate incorporation.

As for C_2H_2, the first three fundamental vibrational modes of H_2 (H_2^{ν} with $\nu=1-3$) are not treated as separate species, although the vibrational excitation of the ground state hydrogen molecules is taken into account in the Boltzmann solver.

d. Electron attachment. Given the difficulty of adding an electron to the filled valence shell of the C_2H_2 molecule, the acetylene anion $C_2H_2^-$ lies at a higher energy than the acetylene neutral ground state, and is thus unstable with respect to autodetachment [40]. A stable C_2H^- anion can, however, be produced by dissociative attachment on C_2H_2, as the ethynyl radical features a sufficiently large electron affinity of approximately 3 eV,

$$C_2H_2 + e \rightarrow C_2H^- + H. \tag{11}$$

A cross section for the dissociative electron capture on C_2H_2 has been proposed by Rutkowsky *et al.* [32], who investigated the negative ion formation for a few simple hydrocarbon molecules in the energy range of 0–15 eV. Two separate peaks with a sharp resonantlike behavior can be distinguished with a first maximum of $\sim 7 \times 10^{-24}$ m^2 around 3 eV, as seen in Fig. 2(a). In spite of the fact that the electron attachment cross section is about three or four orders of magnitude lower than the respective ionization cross sections for the production of positive ions, it can still produce a substantial amount of negative ions in the plasma. Indeed, due to their negative charge the anions will remain confined in the plasma bulk by means of the action of the ambipolar potential and have a longer residence time in the discharge com-

TABLE III. Ion-molecule processes taken into account in the fluid model. The abbreviation "est." stands for estimated, and "calc." for calculated.

	Reaction	Rate constant ($m^3\ s^{-1}$)	Comment	Reference
	Cluster growth through hydrocarbon anions ($C_{2n}H^-$) with C_2H_2			
1.	$C_2H^- + C_2H_2 \rightarrow C_4H^- + H_2$	1.0×10^{-18}	est.	[14]
2.	$C_4H^- + C_2H_2 \rightarrow C_6H^- + H_2$	1.0×10^{-18}	est.	[14]
3.	$C_{2n}H^- + C_2H_2 \rightarrow C_{2n+2}H^- + H_2$	1.0×10^{-18}	$n=3,\ldots,5$,est.	[14]
	Cluster growth through hydrocarbon cations ($C_{2n}H_m^+$) with C_2H_2 or H_2			
4.	$H_2^+ + C_2H_2 \rightarrow C_2H_2^+ + H_2$	5.3×10^{-15}		[41]
5.	$C_2H^+ + H_2 \rightarrow C_2H_2^+ + H$	1.7×10^{-15}		[41]
6.	$C_2H^+ + C_2H_2 \rightarrow C_4H_2^+ + H$	1.2×10^{-15}		[42]
7.	$C_2H_2^+ + C_2H_2 \rightarrow C_4H_2^+ + H_2$	1.2×10^{-15}		[42]
8.	$C_4H_2^+ + C_2H_2 \rightarrow C_6H_4^+$	1.4×10^{-16}		[41]
9.	$C_6H_2^+ + C_2H_2 \rightarrow C_8H_4^+$	1.0×10^{-17}		[42]
10.	$C_6H_4^+ + C_2H_2 \rightarrow C_8H_6^+$	1.0×10^{-16}	est.	[42]
11.	$C_8H_4^+ + C_2H_2 \rightarrow C_{10}H_6^+$	1.0×10^{-16}	est.	[42]
12.	$C_8H_6^+ + C_2H_2 \rightarrow C_{10}H_6^+ + H_2$	1.0×10^{-16}	est.	[42]
13.	$C_{10}H_6^+ + C_2H_2 \rightarrow C_{12}H_6^+ + H_2$	1.0×10^{-16}	est.	[42]
	Neutralization reactions of hydrocarbon anions with H_2^+ and $C_{2n}H_m^+$			
14.	$C_{2n}H^- + H_2^+ \rightarrow C_{2n}H + H + H$	$\sim1.7\times10^{-13}$	$n=1,\ldots,6$ calc.	[43]
15.	$C_{2n}H^- + C_{2n}H_m^+ \rightarrow C_{2n}H + C_{2n}H_m$	$\sim4.0\times10^{-14}$	$n=1,\ldots,6$ calc.	[43]

pared to the other species. Therefore, even modest production rates are capable of producing sufficient anions, which can only be lost in the gas phase either by mutual recombination with a positive ion or by electron detachment [15].

No dissociative attachment on H_2 has been considered, since the formation of H^- anions involves the constraint of two successive reactions leading to a concentration that proved to be insignificant in our calculations [15].

3. General aspects of the chemical clustering reactions

Starting from the small acetylenic compounds a series of chemical reactions has been gradually incorporated in the 1D fluid model that leads to the formation of larger hydrocarbons containing up to a maximum of 12 carbon atoms. Tables III and IV, respectively, delineate the different ion-molecule and molecule-molecule processes that are incorporated in the present model. For the temperature- or pressure-dependent rates the general reaction rate notation is given. The rate constants in Tables III and IV reflect the rates at a gas temperature of 400 K and a gas pressure of 40 Pa. In the following paragraphs the relevance of the various possible particle generation pathways in low-pressure discharges will be discussed in more detail. Figure 3 provides a schematic representation of the main reaction pathways included in the model that underlies the growth of larger hydrocarbons in the acetylene discharge.

4. Reactions involving anions

Negative ion reactions are usually not incorporated in the modeling of hydrocarbon discharges, although the electron attachment to acetylenic compounds and the following incorporation of the anions in neutral molecules can lead to high-mass carbon anions that may finally play an important role in the carbonaceous dust generation. The primary C_2H^- anions, formed through the electron impact dissociative attachment on C_2H_2, can trigger a consecutive chain of polymerization reactions that generally evolves as follows:

$$C_2H^- + C_2H_2 \rightarrow C_4H^- + H_2, \tag{12a}$$

$$C_4H^- + C_2H_2 \rightarrow C_6H^- + H_2, \tag{12b}$$

$$\vdots$$

$$C_{2n}H^- + C_2H_2 \rightarrow C_{2n+2}H^- + H_2, \tag{12c}$$

and is commonly referred to as the Winchester mechanism [10]. According to the spectral pattern of the negative ion mass spectrum, shown in Fig. 1(b), the repeated insertion of acetylene molecules results in an anion sequence with nearly pure carbon anions that peaks at the $C_{2n}H^-$ species. Therefore, similar to anion-neutral reactions in silane discharges [15], every anion-acetylene chain process is accompanied by the extraction of a hydrogen molecule and leads to the production of anions in which the carbon atoms are bound to only one hydrogen atom, thus representing linear polyalkynes that contain alternate single and triple bonds. Due to the pair of strongly bound carbon atoms of the initial acetylene, only even-numbered carbon anions have to be considered.

So far no precise rate coefficients for these anion chain reactions can be found in the literature. Only a theoretical

TABLE IV. Molecule-molecule processes taken into account in the fluid model.

	Reaction	Rate constant ($m^3\ s^{-1}$)	Comment	Reference
		Cluster growth through C_2H insertion		
1.	$C_2H+H_2 \rightarrow C_2H_2+H$	4.9×10^{-19}	$1.82\times10^{-17}\exp(-1443/T)$	[24]
2.	$C_2H+H \rightarrow C_2H_2$	4.1×10^{-16}	$1.66\times10^{-13}T^{-1}$	[25]
3.	$C_2H+C_2H_2 \rightarrow C_4H_2+H$	5.8×10^{-17}		[24]
4.	$C_2H+C_4H_2 \rightarrow C_6H_2+H$	6.6×10^{-17}		[24]
5.	$C_2H+C_{2n}H_2 \rightarrow C_{2n+2}H_2+H$	5.0×10^{-17}	$n=3,\ldots,5$	[18], est.
		Hydrogen insertion		
6.	$H+C_2H_2 \rightarrow C_2H_3$	3.5×10^{-19}	$7.25\times10^{-18}\exp(-1212.7/T)$	[44]
7.	$H+C_4H_2 \rightarrow C_4H_3$	1.2×10^{-18}	$2.82\times10^{+19}T^{-11.67}\exp(-6441/T)$	[25]
8.	$H+C_6H_2 \rightarrow C_6H_3$	1.6×10^{-18}	$7.1\times10^{+15}T^{-10.15}\exp(-6667.6/T)$	[25]
9.	$H+C_{2n}H \rightarrow C_{2n}H_2$	4.1×10^{-16}	$1.66\times10^{-13}T^{-1}$; $n=2,\ldots,6$	[25]
10.	$C_{2n}H+H_2 \rightarrow C_{2n}H_2+H$	4.9×10^{-19}	$1.82\times10^{-17}\exp(-1443/T)$; $n=2,\ldots,6$	[24]
		Hydrogen abstraction		
11.	$H+C_2H_3 \rightarrow H_2+C_2H_2$	6.6×10^{-17}		[44,45]
12.	$H+C_4H_3 \rightarrow H_2+C_4H_2$	2.4×10^{-17}		[25]
13.	$H+C_6H_3 \rightarrow H_2+C_6H_2$	6.6×10^{-17}	$k=k_{reac11}$	[44], est.
		Cluster growth through acetylene insertion		
14.	$C_4H+C_2H_2 \rightarrow C_6H_2+H$	6.6×10^{-17}		[24]
15.	$C_{2n}H+C_2H_2 \rightarrow C_{2n+2}H_2+H$	6.6×10^{-17}	$k=k_{reac14}$; $n=3,\ldots,5$	[24], est.
		Other neutral-neutral reactions		
16.	$CH+H_2 \rightarrow CH_2+H$	1.0×10^{-18}	$1.82\times10^{-22}T^{1.79}\exp(-840.4/T)$	[25]
17.	$CH_2+H \rightarrow CH+H_2$	2.7×10^{-16}		[44,46]
18.	$CH_2+CH_2 \rightarrow C_2H_2+H_2$	5.3×10^{-17}		[25,47]
19.	$C_2H+C_2H_3 \rightarrow C_2H_2+C_2H_2$	5.0×10^{-17}		[48]
20.	$CH_2+CH \rightarrow C_2H_2+H$	6.6×10^{-17}		[25]
21.	$C_2H_2+C_2H \rightarrow C_4H_3$	2.2×10^{-18}	$1.82\times T^{-6.3}\exp(-1404/T)$	[25]
22.	$C_4H_2+C_2H \rightarrow C_6H_3$	2.2×10^{-18}	$k=k_{reac21}$	[25], est.
23.	$C_2H_3+CH \rightarrow C_2H_2+CH_2$	8.3×10^{-17}		[48]
24.	$C_4H_3+H \rightarrow C_2H_2+C_2H_2$	1.1×10^{-16}	$2.65\times10^{-11}T^{-1.6}\exp(-1117/T)$	[25]
25.	$C_6H_3+H \rightarrow C_4H_2+C_2H_2$	8.1×10^{-17}	$3.98\times10^{-11}T^{-1.6}\exp(-1409/T)$	[25]

upper limit can be calculated using the Langevin collision rate coefficient k_L for ion-molecule reactions [49],

$$k_L = e\left(\frac{\pi\alpha_i}{\epsilon_0 m_{ij}}\right)^{1/2} = 2.3\times10^{-15}\left(\frac{\alpha_i}{m_{ij}}\right)^{1/2}\ \mathrm{m^3\ s^{-1}}, \quad (13)$$

where α_i in $Å^3$ represents the polarizability of the neutral atom or molecule i, and m_{ij} is the reduced molecular mass in amu units,

$$m_{ij} = \frac{m_i m_j}{m_i + m_j}, \quad (14)$$

of the two reacting species. Hence, for the repeated insertion of acetylene molecules, with a polarizability of 3.49 $Å^3$ [50], the Langevin formula predicts a maximum rate constant of the order of $10^{-15}\ m^3\ s^{-1}$. Since the Langevin rates are known to overestimate the actual reaction rates, a smaller value should be adopted. Based on the experimental suggestion in [14], the rate coefficient for the anion reactions is set to $10^{-18}\ m^3\ s^{-1}$. Indeed, our calculations have shown that the implementation of larger reaction rates results in an increasing number density of higher-mass hydrocarbon anions, which is not consistent with the decreasing trend observed in the negative ion mass spectrum shown in Fig. 1(b).

In theory the anions can also react with higher-order hydrocarbon molecules ($C_{2n}H_2$). Given that the C_4H_2 concentration, and especially that of higher-mass hydrocarbons, represents at most a few percent of the gas mixture, these reactions are not considered in the present model due to their insignificant contribution in comparison to reactions with acetylene.

5. Reactions involving cations

In contrast to silane plasmas, no kinetic bottleneck prevents the formation of larger hydrocarbon positive ions that appear to polymerize to the same extent as the negative ions (see Fig. 1) and the positive ion route can thus not be disre-

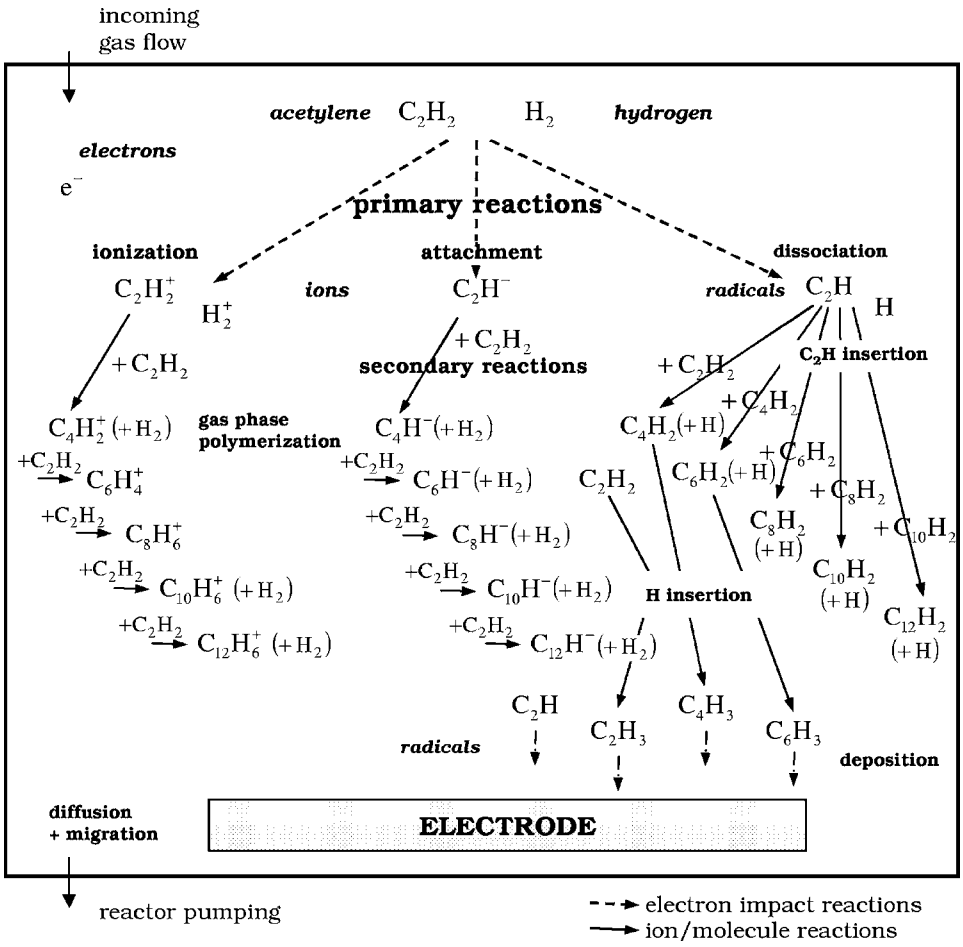

FIG. 3. Schematic representation of the main reaction pathways underlying the growth of larger hydrocarbons in the acetylene discharge.

garded as a possible additional pathway toward carbonaceous dust formation. Ionization of acetylene creates mostly $C_2H_2^+$ ions that have a marked tendency to undergo further condensation reactions with C_2H_2 leading to the production of larger hydrocarbon cations. The principal ionic condensation pathway can be summarized by

$$C_2H_2^+ \xrightarrow{+C_2H_2} C_4H_2^+_{(+H_2)} \xrightarrow{+C_2H_2} C_6H_4^+ \xrightarrow{+C_2H_2} C_8H_6^+ \xrightarrow{+C_2H_2} C_{10}H_6^+_{(+H_2)} \xrightarrow{+C_2H_2} \cdots, \tag{15}$$

where for any given ion-acetylene reaction the degree of hydrogenation and thus the specific ionic product seems to depend on the carbon number within the molecule and is determined by the extent of collisional stabilization and subsequent breakdown of the chemical intermediate [21]. Identical condensation reactions have also been invoked as a potential nucleation pathway in the soot formation chemistry of hydrocarbon flames and may also play an important role in the interstellar media.

The reaction of $C_2H_2^+$ with C_2H_2 produces the intermediate $[C_4H_4^+]^*$ which decomposes predominantly into $C_4H_2^+$ and $C_4H_3^+$ [21]. The separate production of $C_4H_3^+$ is, however, not considered in our model since it is inherently incorporated in the $C_4H_2^+$ generation by taking the overall reaction rate constant of both reaction channels, i.e., 1.2×10^{-15} m^3 s^{-1} [42]. It should be noted that another fragment ion generated from acetylene ionization, i.e., C_2H^+, also reacts with C_2H_2 to give $C_4H_2^+$,

$$C_2H^+ + C_2H_2 \rightarrow C_4H_2^+ + H \tag{16}$$

with the fast rate constant of 1.2×10^{-15} m^3 s^{-1} [42]. Further, since electron impact ionization on C_6H_2 also generates $C_6H_2^+$ ions, two separate reactions have been included for hydrocarbons containing six carbon atoms,

$$C_6H_2^+ + C_2H_2 \rightarrow C_8H_4^+, \tag{17a}$$

$$C_6H_4^+ + C_2H_2 \rightarrow C_8H_6^+, \tag{17b}$$

which lead to the respective production of $C_8H_4^+$ and $C_8H_6^+$. No particular data on the reaction product of ionic condensation reactions with larger hydrocarbons cations exist. Therefore, for every cation containing more than six carbon atoms (i.e., $C_{2n}H_m^+$ with $n>3$) the specific ionic product, and thus the number (m) of hydrogen atoms assumed in our model, is based on the most relevant peak that is present in the cation mass spectrum at the corresponding carbon atom number $2n$ [see Fig. 1(a)]. As for the anions, the positive ion mass spectrum shows a clear dominance of species with an even carbon atom number which seems to peak at hydrocarbon cations having a relatively low hydrocarbon content. Based on the slowly decreasing reactivity observed in the successive condensation reactions, the reaction rate coeffi-

cient of the larger positive ions has been estimated to be around 1.0×10^{-16} m^3 s^{-1}.

The ionic fragments C^+, CH^+, and C_2^+, formed through dissociative ionization of acetylene, can also react with C_2H_2 via condensation with loss of H or H_2, forming C_3H^+, $C_3H_2^+$, and C_4H^+, respectively. Although all reactions are rapid with rate constants close to the collision limit, these reactions are not taken into account in the model, since the concentration of the reacting ions is too low to provide for a significant contribution.

6. Ion-ion mutual neutralization

Besides fast polymerization reactions, positive and negative ions can undergo mutual neutralization, which represents the most significant loss mechanism for the anions since they are not able to reach the reactor walls due to the positive plasma potential. The rate constant k_N of the general mutual neutralization

$$X^+ + Y^- \rightarrow X + Y \tag{18}$$

is only weakly dependent on the nature of the ion [49]. An appropriate scaling formula as a function of the electron affinity A_e of the parent neutral radical of the anion and the ion-ion reduced mass m_{ij} has been derived by Hickman [43],

$$k_N = 5.34\times10^{-13}\times A_e^{-0.4}\times m_{ij}^{-0.5}\left(\frac{T_{gas}}{300}\right)^{-0.5}\ \text{m}^3\ \text{s}^{-1}, \tag{19}$$

in which T_{gas} is the gas temperature in kelvin and A_e and m_{ij} are in eV and amu units, respectively. The corresponding electron affinities are taken from [51] and seem to be quite large, being in the range of 2–4.4 eV.

Anion neutralization with H_2^+ and every hydrocarbon positive ion has been taken into account (see Table III, reactions 14 and 15). In our model the neutralized forms of the larger hydrocarbon cations ($C_mH_n^+$ with $m\geqslant6$ and $n\geqslant4$) are not explicitly considered as they are assumed to diffuse back into the background gas. Based on the formula derived by Hickman H_2^+ seems to be the most efficient collision partner. A further small spread in the reaction rate coefficients of the anions with a certain cation can be observed: a decreasing trend for k_N with the extent of anion polymerization directly follows from the increase in electron affinity with the number of carbon atoms.

7. Neutral collisions and C_2H insertion reactions

Gas phase reactions between neutrals can also produce higher-molecular-weight compounds. The ethynyl radical C_2H, produced by dissociation of acetylene, is known to be a very reactive intermediate which may eventually initiate a polymerization process. Insertion of C_2H into C_2H_2 first produces diacetylene and atomic hydrogen through the following condensation reaction:

$$C_2H + C_2H_2 \rightarrow C_4H_2 + H. \tag{20}$$

The diacetylene forms then the basis for the production of large polyunsaturated hydrocarbon molecules $C_{2n}H_2$ by further insertion of C_2H,

$$C_2H + C_{2n}H_2 \rightarrow C_{2n+2}H_2 + H. \tag{21}$$

Note that the additional production of C_4H_2 molecules through recombination of two reactive ethynyl radicals seems to be excluded by shock-tube studies [52].

For the larger $C_{2n}H_2$ molecules a corresponding $C_{2n}H$ radical can be generated by electron-induced C-H bond breakage (see Table II) which may play an important role in the deposition process. Other radicals that are important for film growth, e.g., $C_{2n}H_3$, are produced from the polyacetylene $C_{2n}H_2$ molecules by hydrogen insertion. Due to the presence of a large amount of atomic hydrogen from the dissociation of H_2, these types of processes cannot be excluded from our model.

8. Role of aromatic compounds

So far only reactions with linear polyalkyne carbon chains have been considered, since the tendency to aromatic ring generation in low-temperature hydrocarbon plasmas still remains an open issue. In high-resolution mass spectrometry measurements the emergence of hydrocarbons including six carbons and a larger number of hydrogen atoms might be interpreted as a change in carbon cluster structure. In order to investigate the possible role of aromatic compounds in hydrocarbon plasmas and their subsequent role in dust growth, data on the aromatic chemistry are needed, which seem to be unavailable for low-temperature plasmas. Polycyclic aromatic hydrocarbon (PAH) formation has, on the other hand, long been investigated in astrophysical environments and in particle soot formation during combustion of hydrocarbon flames. Frenklach *et al.* [24,25,53] developed a comprehensive chemical kinetic model that describes the initial aromatic ring formation and further PAH growth through the hydrogen-abstraction-C_2H_2-addition (HACA) reaction mechanism in hydrocarbon flames.

However, many of the kinetic constants for the aromatic compound formation reported in the literature were estimated only at the high temperatures and pressures that are of interest for pyrolysis and soot formation, while the plasmas commonly used for the deposition of carbon films usually operate at very low pressures (e.g., 0.001–1.0 Torr) and at much lower gas temperatures (in the order of 300–500 K). Therefore, large uncertainties in the rate coefficients often exist and a systematic investigation of all the rate coefficients would be beyond the scope of the present paper. Furthermore, when applied to much lower pressures in circumstellar environments, kinetic models predict a very limited growth of aromatic compounds, i.e., the growth seems only to effectively take place in the relatively narrow high-temperature window of 900–1100 K [54]. Therefore, since the role of cyclic ring generation in the carbonaceous dust production of hydrocarbon plasmas is still unclear and due to the uncertainty arising from the usage of reaction pathways and rate coefficients from the combustion literature, aromatic compounds have not been included in the plasma chemistry model.

C. Diffusion and wall deposition losses

Besides chemical reactions in the gas phase, species can also be lost by diffusion to the discharge walls followed by

TABLE V. Overview of the Lennard-Jones parameters and polarizabilities of some hydrocarbon species [50,56].

Molecule	σ (Å)	ϵ/k_B (K)	α (Å)^3
C_2H_2	4.033	231.8	3.49
H_2	2.827	59.7	0.819
H	2.708	37.0	
CH	3.370	68.6	
CH_4	3.758	148.6	2.60
C_2H_4	4.163	224.7	4.22
C_6H_6	5.349	412.3	10.4

deposition, i.e., plasma-wall interaction. In order to obtain the overall diffusion coefficient D_j in $m^2\,s^{-1}$ of a neutral species j, we first need to determine the binary diffusion coefficients D_{ij} in every background gas i (in this case C_2H_2 and H_2) [49],

$$D_{ij} = \frac{3}{16}\frac{k_B T_{gas}}{p_{tot}}\frac{(2\pi k_B T_{gas}/m_{ij})^{1/2}}{\pi\sigma_{ij}^2\Omega_D(\Psi)}, \tag{22}$$

where k_B is the Boltzmann constant, T_{gas} is the gas temperature in kelvin, p_{tot} is the total gas pressure in pascals, m_{ij} is the reduced molecular mass in amu, σ_{ij} is the binary collision diameter in Å,

$$\sigma_{ij} = \frac{\sigma_i + \sigma_j}{2}, \tag{23}$$

and $\Omega_D(\Psi)$ is the diffusion collision integral given by [49]

$$\Omega_D = \frac{A}{\Psi^B} + \frac{C}{e^{D\Psi}} + \frac{E}{e^{F\Psi}} + \frac{G}{e^{H\Psi}} \tag{24}$$

with $\Psi = T_{gas}/\epsilon_{ij}$, $\epsilon_{ij} = (\epsilon_i \times \epsilon_j)^{0.5}$, and constants $A = 1.060\,36$, $B = 0.156\,10$, $C = 0.193\,00$, $D = 0.476\,35$, $E = 1.035\,87$, $F = 1.529\,96$, $G = 1.764\,64$, and $H = 3.894\,11$.

The overall diffusion coefficient D_j can then be calculated by Blanc's law [55],

$$\frac{p_{tot}}{D_j} = \sum_i \frac{p_i}{D_{ij}}, \tag{25}$$

where the summation is over every background gas i.

The Lennard-Jones parameters σ_i and ϵ_i, i.e., the collision diameter of the species and its potential energy, respectively, are listed in Table V for a few simple hydrocarbon molecules and radicals [56]. Based on these data, the values of other species have been estimated. The parameters for C_2H_3 were for example obtained by linear interpolation between C_2H_2 and C_2H_4, whereas those for CH_2 were estimated by linear interpolation between CH and CH_4.

For the ions both a mobility and a diffusion coefficient need to be considered. The ion mobility of an ionic species j in the background gas i (in $m^2\,V^{-1}\,s^{-1}$) can be calculated from the low-electric-field Langevin mobility expression [55]

$$\mu_{ij} = 0.514 m_{ij}^{0.5}\frac{T_{gas}}{p_{tot}}\alpha_i^{-0.5}, \tag{26}$$

where α_i in Å^3 represents the polarizability of the background gas i, also given in Table V and taken from [50]. The overall ion mobility μ_j can then again be obtained by Blanc's law. Finally, the ion diffusion coefficient can be derived from the Einstein relation

$$D_j^{\pm} = \frac{k_B T_{ion}}{e}\mu_j \tag{27}$$

where T_{ion} represents the ion temperature, which is assumed to be equal to the gas temperature T_{gas}.

The plasma-wall interaction is described by means of a sticking model that ensures that the deposition of species at the walls is taken into account, albeit in a simplified manner. For every species the surface reaction probability is expressed in terms of a sticking coefficient. The model assumes that only the radicals react with the surface, while acetylene and the larger polyunsaturated $C_{2n}H_2$ molecules are reflected back into the discharge. For the C_2H_3, C_4H_3, and C_6H_3 radicals, the surface sticking coefficient is set to 0.35 [57], while the CH and CH_2 species have a smaller sticking probability of 0.025 [58]. Ethynyl radicals (C_2H) are very reactive toward the surface, resulting in a sticking coefficient of 0.9 [57]. Although no information on the reaction probability of larger polyacetylene radicals $C_{2n}H$ ($n=2-6$) exists, a decrease in plasma-wall reactivity can be expected as the radical mostly sticks to the surface with the outer non-hydrogen-carrying carbon atom, which becomes less reachable when the size of the impinging radical increases. Due to their similar structure, the sticking coefficients of larger $C_{2n}H$ radicals are therefore estimated from the sticking coefficient of the ethynyl radicals, by gradually decreasing the reactivity with increasing size.

Besides their incorporation into the depositing layer, a fraction of every $C_{2n}H$ radical recombines with a hydrogen atom at the walls and is reemitted into the plasma under the form of a $C_{2n}H_2$ molecule. The radicals that mostly dominate the film growth are $C_{2n}H_3$ and C_2H [18,59]. Note that although ethynyl radicals have a much larger sticking coefficient, the deposition process will have to compete with the fast C_2H insertion reactions in the plasma, resulting in a lower number density for C_2H in comparison to number densities of the $C_{2n}H_3$ molecules (see below in Fig. 6).

Besides the radicals, positive ions can also play a role in the deposition process and their sticking coefficient is assumed to be equal to 1. Due to their negative charge, the anions, however, are not able to reach the reactor walls and hence they do not play a direct role as a depositing species.

Finally, note that when a hydrocarbon radical sticks to the surface, only 10% of the hydrogen will be incorporated into the layer. Any additional hydrogen will flow back to the discharge under the form of molecular hydrogen. Hence, every radical adsorption is immediately followed by an adequate amount of H_2 desorption from the surface.

III. RESULTS AND DISCUSSION

Results presented here are computed for typical conditions that result in particle formation. The conventional PECVD reactor has a parallel-plate discharge geometry with an interelectrode gap of 3 cm. The upper electrode (at 3 cm) is capacitively coupled to the rf power supply with a driving frequency of 13.56 MHz, while the lower electrode (at 0 cm) remains electrically grounded. 20 sccm of pure C_2H_2 is fed into the discharge, which is operated at a low pressure of approximately 40 Pa or 0.3 Torr, a power of 5 W, and a uniform gas temperature of 400 K.

In the first section the results obtained from the discharge model presented above are discussed at the reported discharge conditions and include the density profiles of all species listed in Table I. The deduction of theoretical mass spectra from the positive and negative ion fluxes will be described in Sec. III B, whereas in the last section the role of hydrogen dilution will be discussed.

A. Concentration profiles of the various species

The calculated time-averaged profiles of the electron and most important ion concentrations are represented in Fig. 4. For clarity, the positive and negative ion density profiles have been plotted separately. The electron number density is displayed on the anion plot in Fig. 4(b) and takes a value of about 5×10^{14} m^{-3}. Due to the occurrence of a time variation near the plasma boundaries, period-averaged ion and electron concentrations have been depicted.

For the positive ions, only the most significant concentration profiles are shown in Fig. 1(a). Ionic C_2H_2 fragments reaching a concentration of approximately 10^{10}–10^{11} m^{-3}, such as H^+, C_2H^+, CH^+, C_2^+, and C^+, are not represented on the plot. For clarity, labels 6, 8, and 10 denote the $C_6H_4^+$, $C_8H_6^+$, and $C_{10}H_6^+$ species, respectively. The most dominant carbonaceous cation is found to be $C_4H_2^+$ followed by $C_6H_2^+$ and $C_6H_4^+$. This result is consistent with the most abundant positive ions observed in the cation mass spectrum, which seems to peak at C_4 and C_6 containing ions [see Fig. 1(a)]. Since the largest species considered in our model contain 12 carbon atoms, the clustering processes are stopped at $C_{12}H_6^+$ cations, which can, hence, only be lost by neutralization reactions in the gas phase or by drift and diffusion toward the reactor walls. Therefore, this species attains a concentration of the order of 1.2×10^{16} m^{-3} and symbolizes the summation of all larger cations. Note that ionic profiles from the principal condensation pathway (i.e., $C_2H_2^+\rightarrow C_4H_2^+\rightarrow C_6H_4^+\rightarrow C_8H_6^+\rightarrow C_{10}H_6^+\rightarrow\ldots$) exhibit a lower density in the plasma bulk. This decrease in density is a direct consequence of the loss of species due to fast polymerization reactions with C_2H_2 that cannot be as quickly compensated by the slow movement of positive ions toward the plasma center. The last $C_{12}H_6^+$ density plot does not reveal this specific shape, since no reaction is included that leads to the formation of a $C_{14}H_8^+$ succeeding cation. Finally, the H_2^+ ions, formed by ionization of H_2, also react with C_2H_2 at a rate close to the collision limit (see reaction 4, Table III) and obtain a density that is more than two orders of magnitude lower than the $C_2H_2^+$ density, i.e., 2×10^{11} m^{-3} [not shown in Fig. 4(a)].

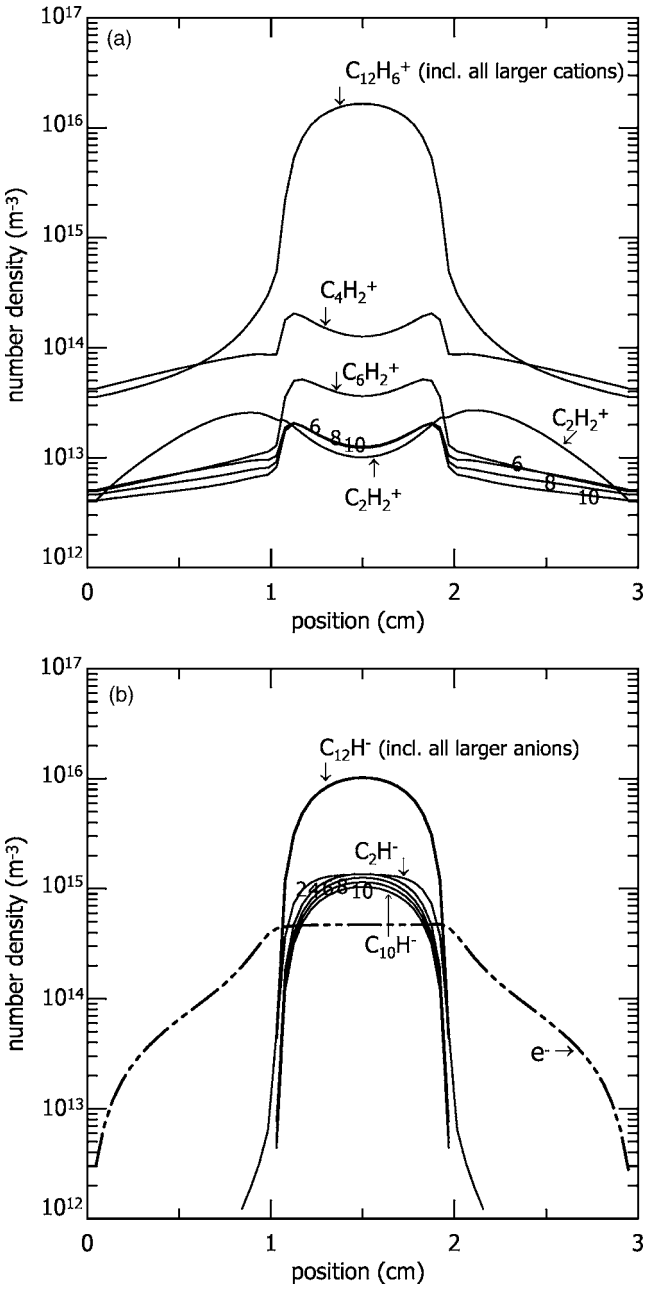

FIG. 4. Computed number density profiles of the ions and electrons in a capacitive rf acetylene discharge operated at 13.56 MHz, 40 Pa, and 5 W: (a) positive ions; (b) anions and electrons. In (a) the numbers 6, 8, and 10 symbolize the $C_6H_4^+$, $C_8H_6^+$, and $C_{10}H_6^+$ cations, respectively, while the numbers 2–10 in (b) refer to the corresponding $C_{2n}H^-$ anion.

A second pathway involving negative ions can be distinguished in the anion plot in Fig. 1(b). The label on every concentration profile refers to the number of carbon atoms present in the respective $C_{2n}H^-$ anion. Due to their negative charge, all anions are confined to the center of the plasma and are almost absent in the plasma sheaths. Apart from the last accumulating stage, i.e., $C_{12}H^-$, a general decreasing trend can be observed with increasing carbon atom number,

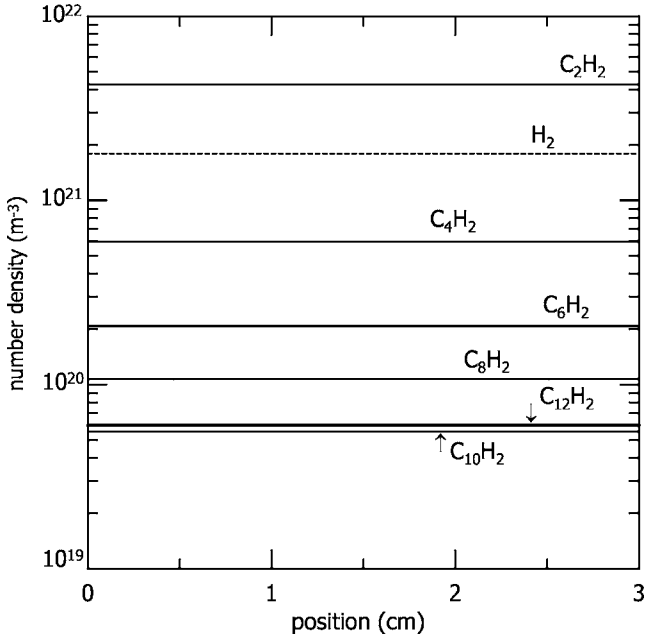

FIG. 5. Calculated number density profiles of C_2H_2, H_2, and the parent higher-order hydrocarbon molecules $C_{2n}H_2$ in a capacitive rf acetylene discharge operated at 13.56 MHz, 40 Pa, and 5 W.

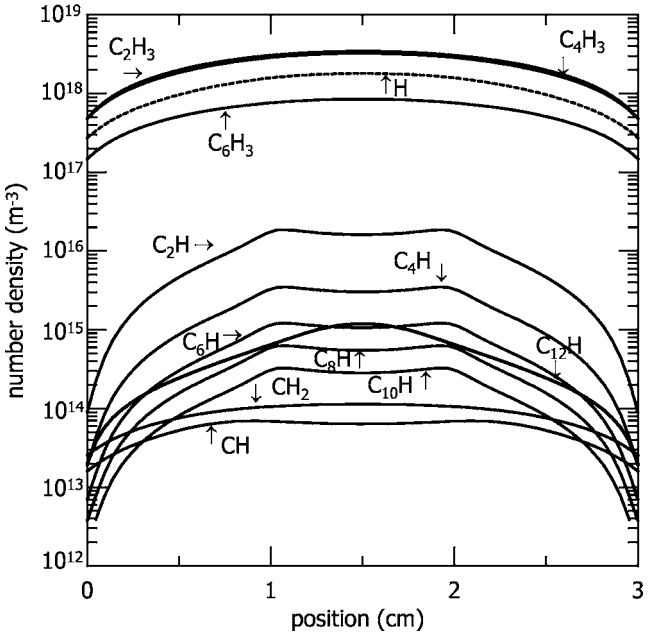

FIG. 6. Calculated number density profiles of the various hydrocarbon radicals in a capacitive rf acetylene discharge operated at 13.56 MHz, 40 Pa, and 5 W.

which is in good agreement with the experimental observations shown in Fig. 1(b) and in [36] where the same trend can be detected. Similar to $C_{12}H_6^+$, no subsequent growth of $C_{12}H^-$ to larger anions has been incorporated, and its formation yield is therefore around one order of magnitude higher than the smaller negative ions. In this case mutual neutralization with mainly the most abundant $C_{12}H_6^+$ and $C_4H_2^+$ positive ions forms the only possible loss process. In contrast to the cation plot, the repetitive insertion of acetylene in the consequent $C_{2n}H^-$ anion advances at the slower rate constant of 10^{-18} m^3 s^{-1}, resulting in the production of higher concentrations of intermediate hydrocarbon negative ions in comparison to the intermediates in the cation chain, where all reactions proceed at a rate close to the collision limit (see reactions in Table III). The total sum of all positive and negative ions, however, remains the same.

Hence, from the above we can conclude that two different pathways involving either hydrocarbon positive or negative ions can be distinguished which can lead to the formation of higher-order hydrocarbon cations and anions, respectively. Thus both positive ions, starting from $C_2H_2^+$, and negative ions, starting from C_2H^-, may participate as precursors in the initial stage of particle formation in acetylene discharges. One major difference is, however, that the negatively charged species will remain trapped in the discharge due to the action of the ambipolar potential, resulting in much longer residence times that favor their further growth toward nano- and micrometer-sized particles. The positive ions, on the other hand, can be efficiently evacuated over the plasma sheaths. Hence, the positive ion clustering sequence will have to compete with the efficient loss of cations toward the reactor walls and thus the subsequent smaller residence times of the positive ions in the plasma, which are generally of the order of 10^{-5} s. When the particles eventually reach the nanometer area they will in any case acquire a negative charge due to the collection of plasma ions and electrons [27].

The concentrations of molecular hydrogen and the most important hydrocarbon molecules, i.e., C_2H_2 and $C_{2n}H_2$ (with $n>1$) are provided in Fig. 5. Due to their unreactivity at the discharge walls, the density profiles are homogeneously distributed throughout the entire reactor and generally exceed the radical concentrations, shown in Fig. 6. The highest gaseous products present in the C_2H_2 discharge are acetylene (C_2H_2), diacetylene (C_4H_2), and molecular hydrogen (H_2). The densities of these species are around one order of magnitude higher in comparison to the larger unsaturated polyacetylenes with the general formula $H—(C\equiv C)_n—H$ (with $n=3,\ldots,6$). The feedstock gas C_2H_2 is present at the highest density and takes a value of about 4×10^{21} m^{-3}. Although molecular hydrogen is not fed into the reactor, the H_2 molecules also exhibit a relatively high density of roughly 1.8×10^{21} m^{-3}. This is due to the fact that many of the chemical reactions shown in Tables III and IV lead to the extraction of molecular hydrogen. Further H_2 production is also provided from H_2 release at the discharge walls due to the plasma-wall interactions of various hydrocarbon radicals (see above). For the larger polyunsaturated hydrocarbon molecules, the diacetylene generation especially cannot be neglected. This finding is in contrast with the neutral products found in methane, ethane, and ethylene systems, where for the neutral compounds no species containing more than two carbon atoms can be detected [16,21]. In the present acetylene discharge, C_4H_2 is found to comprise about 4% of the total gas mixture. The presence of these high concentrations of larger neutral gas products in acetylene discharges has also been measured in the mass spectrometry studies of Doyle [18] and Vasile *et al.* [21]. Again, apart from the final accumulating stage (i.e., $C_{12}H_2$), a general decreasing trend

for the higher-mass hydrocarbons can be observed, where $C_{2n}H_2$ is generated through the repetitive insertion of C_2H in the previous $C_{2n-2}H_2$ hydrocarbon molecule (see Fig. 3 or reactions 1–5 in Table IV).

Finally, radicals exhibiting a decreasing concentration profile toward the reactor walls are illustrated in Fig. 6. Besides the occurrence of mainly carbon-rich species (C_nH_m with $n>m$), atomic hydrogen, produced from molecular hydrogen dissociation and chemical hydrogen abstraction reactions, seems to be present at the relatively high amount of 2×10^{18} m^{-3}. For the carbonaceous species, $C_{2n}H_3$ (with $n=1-3$) are the most important radicals in the acetylene discharge, exhibiting a density of the order of 3.5×10^{18} m^{-3} (C_2H_3 and C_4H_3) and 8.7×10^{17} m^{-3} (C_6H_3). These large amounts of $C_{2n}H_3$ radicals are also found in experimental measurements of low-pressure acetylene reactors [18,60], and, hence, imply that the $C_{2n}H_3$ can play a dominant role in the film growth. Although the ethynyl radicals (C_2H) obtain a much lower number density in the plasma bulk (i.e., 1.6×10^{16} m^{-3}), these species will also largely contribute to the film growth due to their very high plasma-wall reactivity, which is envisioned by their steep decline toward the discharge surface. The small decrease in the density profiles of all $C_{2n}H$ radicals ($n=1-5$) at the plasma center can again be attributed to fast C_2H_2 insertion reactions. $C_{12}H$, on the other hand, can only be lost by deposition at the walls and by reactor pumping. Finally, the smallest hydrocarbon radicals methylidyne (CH) and methylene (CH_2) are present in the nominal amounts of 6.7×10^{13} and 1.1×10^{14} m^{-3}, respectively, and show the least reactivity at the plasma walls.

B. Positive and negative ion mass spectra

From the fluxes of the positive ions toward the reactor walls we can deduce a theoretical positive ion mass spectrum, which is depicted in Fig. 7. It includes all the incorporated positive ions of our model and ranges up to 150 amu. Since the number of species in our model is limited, the variation in the hydrogen content of the large molecules is less than in the experiment. Note that every peak in the spectrum is normalized with respect to the $C_4H_2^+$ hydrocarbon cation, which has the maximum intensity. A quantitative comparison with the experimental mass spectrum of Deschenaux *et al.* [Fig. 1(a)] provides for a relatively good agreement, where the maximum amplitude for even carbon atom numbers is often separated by a mass difference of 24 amu: 26-50-74 and 102-126-150. The calculated $C_2H_2^+$ peak relates almost in the same way to the $C_4H_2^+$ peak and a comparable decreasing trend toward larger hydrocarbon positive ions can be detected. We have to bear in mind, however, that the experimentally obtained plots by Deschenaux *et al.* are uncorrected for any mass-dependent falloff in the sensitivity of the spectrometer, which may lead to discrepancies at higher masses in the spectrum. Note that the masses 43 and 59 in the experimental mass spectra represent acetone (CH_3-O-CH_3) impurity, which is often used to stabilize the acetylene gas.

For the negative ions a correct anion flux can only be obtained when the discharge is switched off (i.e., by applying a zero rf voltage in our model) in order to enable the negatively charged species to escape from the discharge. Similarly, experimental mass spectrometry can only detect negative ions in the pulsed discharge mode, where the modulation frequency has to be below 10 kHz such that the discharge sheaths have sufficient time to collapse [36]. Figure 8 displays the theoretical anion mass spectrum, where all peaks have been normalized with respect to the C_2H^- peak. Exact agreement with the measured spectrum is not reached, because the calculated C_2H^- and C_4H^- peaks appear to be over-

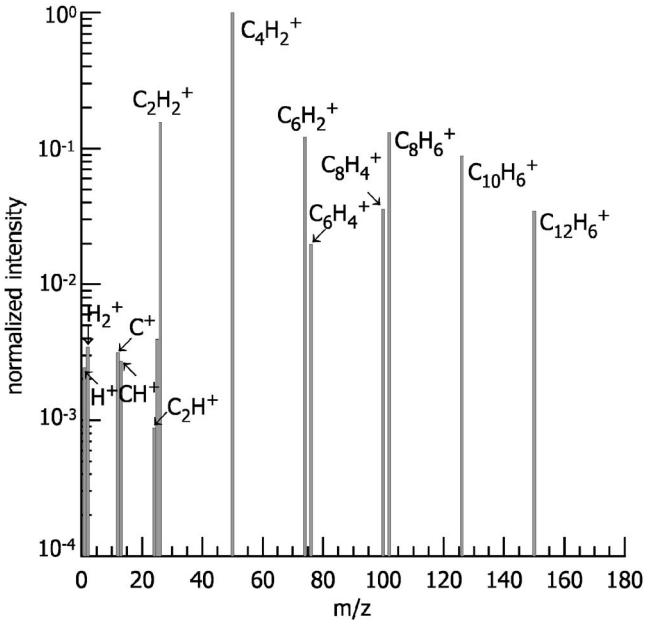

FIG. 7. Normalized positive ion mass spectrum computed from the fluxes of the positive ions toward the reactor wall.

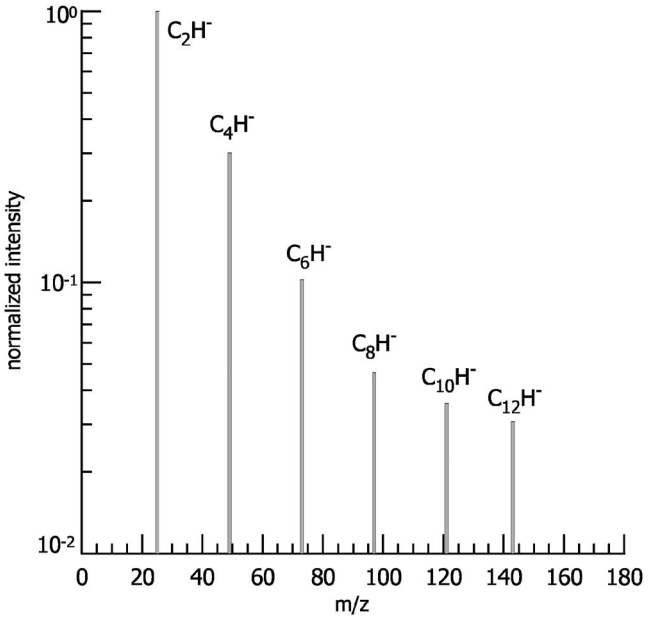

FIG. 8. Normalized negative ion mass spectrum computed from the fluxes of the negative ions toward the reactor wall in a plasma reactor where the rf power was switched off.

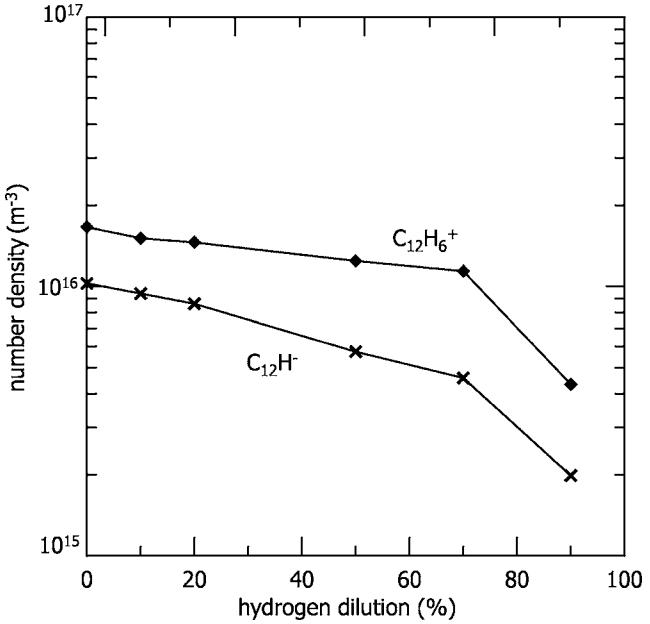

FIG. 9. Variation of the calculated highest polymerized ion densities as a function of molecular hydrogen dilution, keeping the absolute acetylene gas flow and all other discharge operating conditions constant.

estimated. However, the gradually decreasing trend toward higher polymerized anions can again be detected.

C. Hydrogen dilution

In this last section the role of molecular hydrogen on the polymerization process is investigated. We have already shown that even without the introduction of an additional molecular hydrogen gas flow, H_2 molecules are found in very large quantities in acetylene discharges (see Fig. 5). In order to assess the effect of hydrogen dilution on the yield of highly polymerized ions, calculations have been performed for six different amounts of hydrogen dilution. In Fig. 9 the calculated bulk densities of the highest polymerized ions of the positive and negative ion polymerization pathway, i.e., $C_{12}H_6^+$ and $C_{12}H^-$, are plotted as a function of hydrogen dilution. The result clearly shows that for the same operating conditions and the same absolute acetylene gas flow, a higher molecular hydrogen dilution decreases the abundancies of the higher-order hydrocarbon ions. Molecular hydrogen, and indirectly also atomic hydrogen, can thus have a strong influence on the plasma chemistry and on the particle growth. The suppression of higher-mass hydrocarbon ions has also been experimentally observed under similar conditions in [61] and in inductively coupled acetylene discharges where the flowing afterglow of a second molecular hydrogen discharge is used to inject atomic hydrogen into the main plasma vessel [62]. Hydrogen can thus act as an inhibitor on the successive polymerization reactions and may be efficiently used as a suppression method for the production of undesirable contaminants in certain technological applications.

IV. SUMMARY AND CONCLUSIONS

A detailed chemical kinetics scheme has been developed in order to predict the first stage of carbonaceous dust formation in a capacitively coupled rf acetylene discharge. In the applied 1D fluid model the nucleation chemistry is described by 92 volume reactions involving 20 neutral (molecules and radicals) and 21 charged species (positive ions, negative ions, and electrons). Due to the pair of strongly bound carbon atoms of the initial acetylene molecule that persists upon successive integration of acetylene in larger building units, mainly even-numbered hydrocarbons ($C_{2n}H_m$) have been incorporated that include up to a maximum of 12 carbon atoms. Several possible routes that may underlie the carbonaceous dust growth have been discussed. First electron-induced reactions (ionization, dissociation, attachment, and vibrational excitation) determine the decomposition of the C_2H_2 feed gas toward reactive precursors, which can then trigger the formation of larger hydrocarbon species by means of consecutive polymerization reactions that generally evolve by the stepwise insertion of acetylene molecules.

From our model it was found that both positive ions, starting from $C_2H_2^+$, and negative ions, starting from C_2H^-, may participate as precursors in the initial stage of particle formation in acetylene discharges, since both species can lead to the same substantial buildup of highly polymerized cations and anions, respectively. Anions, however, will remain trapped in the plasma due to their negative charge and have thus a larger chance to finally end up in powder formation. The acquired results have also been compared with the experimentally observed mass spectra of Deschenaux *et al.*, where the same trends and thus a relatively good agreement could be observed.

Finally, in concurrence with experimental measurements, a larger amount of hydrogen dilution causes a decrease in the densities of the highest polymerized positive and negative ions. This suggests that molecular hydrogen acts as an inhibitor on the successive polymerization reactions that lead to the formation of higher-mass hydrocarbon ions.

ACKNOWLEDGMENTS

This research was financed by a grant of the Institute for the Promotion of Innovation through Science and Technology in Flanders (IWT-Vlaanderen). W.G. received support from the European Communities under the contract of association between EURATOM and FOM, within the framework of the European Fusion Program, and with financial support from NWO. We acknowledge Professor R. Gijbels for the interest he has shown in this work.

[1] A. Grill, Wear **168**, 143 (1993).
[2] B. K. Daniels, D. W. Brown, and F. M. Kimock, J. Mater. Res. **12**, 2485 (1997).
[3] J. Robertson, Mater. Sci. Eng., R. **37**, 129 (2002).
[4] A. N. Obraztsov, A. P. Volkov, K. S. Nagovitsyn, K. Nishimura, K. Morisawa, Y. Nakano, and A. Hiraki, J. Phys. D **35**, 357 (2002).
[5] S. V. Vladimirov and K. Ostrikov, Phys. Rep. **393**, 175 (2004).
[6] J. Robertson, Thin Solid Films **296**, 61 (1997).
[7] A. Matthews and S. S. Eskildsen, Diamond Relat. Mater. **3**, 902 (1994).
[8] Y. Lifshitz, Diamond Relat. Mater. **8**, 1659 (1999).
[9] P. R. Goglia, J. Berkowitz, J. Hoehn, A. Xidis, and L. Stover, Diamond Relat. Mater. **10**, 271 (2001).
[10] K. Ostrikov, Rev. Mod. Phys. **77**, 489 (2005).
[11] N. S. Xu and S. E. Huq, Mater. Sci. Eng., R. **48**, 47 (2005).
[12] A. A. Fridman, L. Boufendi, T. Hbid, B. V. Potapkin, and A. Bouchoule, J. Appl. Phys. **79**, 1303 (1996).
[13] U. V. Bhandarkar, M. T. Swihart, S. L. Girshick, and U. R. Kortshagen, J. Phys. D **33**, 2731 (2000).
[14] J. Perrin, C. Böhm, R. Etemadi, and A. Lloret, Plasma Sources Sci. Technol. **3**, 252 (1994).
[15] K. De Bleecker, A. Bogaerts, R. Gijbels, and W. Goedheer, Phys. Rev. E **69**, 056409 (2004).
[16] Ch. Deschenaux, A. Affolter, D. Magni, Ch. Hollenstein, and P. Fayet, J. Phys. D **32**, 1876 (1999).
[17] S. Hong, J. Berndt, and J. Winter, J. Phys. D **12**, 46 (2003).
[18] J. R. Doyle, J. Appl. Phys. **82**, 4763 (1997).
[19] D. Herrebout, A. Bogaerts, R. Gijbels, W. J. Goedheer, and A. Vanhulsel, IEEE Trans. Plasma Sci. **31**, 659 (2003).
[20] S. Stoykov, C. Eggs, and U. Kortshagen, J. Phys. D **34**, 2160 (2001).
[21] M. J. Vasile and G. Smolinsky, Int. J. Mass Spectrom. Ion Phys. **24**, 11 (1977).
[22] J. D. P. Passchier and W. J. Goedheer, J. Appl. Phys. **73**, 1073 (1993).
[23] K. De Bleecker, A. Bogaerts, W. Goedheer, and R. Gijbels, IEEE Trans. Plasma Sci. **32**, 691 (2004).
[24] M. Frenklach and J. Warnatz, Combust. Sci. Technol. **51**, 265 (1987).
[25] H. Wang and M. Frenklach, Combust. Flame **110**, 173 (1997).
[26] L. J. Allamandola, A. G. G. M. Tielens, and J. R. Barker, Astrophys. J., Suppl. Ser. **71**, 733 (1989).
[27] K. De Bleecker, A. Bogaerts, and W. Goedheer, Phys. Rev. E **70**, 056407 (2004).
[28] K. De Bleecker, A. Bogaerts, and W. Goedheer, Phys. Rev. E **71**, 066405 (2005).
[29] A. L. Alexandrov and I. V. Schweigert, Plasma Sources Sci. Technol. **14**, 209 (2005).
[30] R. K. Janev and D. Reiter, Phys. Plasmas **11**, 780 (2004).
[31] H. Tawara, Y. Itikawa, H. Nishimura, H. Tanaka, and H. Nakamura, Report No. NIFS-DATA-6, Nagano University, Japan, 1990 (unpublished).
[32] J. Rutkowsky, H. Drost, and H. J. Spangenberg, Ann. Phys. **7**, 259 (1980).
[33] H. Tawara and T. Kato, At. Data Nucl. Data Tables **36**, 167 (1987).
[34] H. Ehrhardt, L. Langhans, F. Linder, and H. S. Taylor, Phys. Rev. **173**, 222 (1968).
[35] A. G. Engelhardt and A. V. Phelps, Phys. Rev. **131**, 2115 (1963).
[36] Ch. Hollenstein, W. Schwarzenbach, A. A. Howling, C. Courteille, J.-L. Dorier, and L. Sansonnens, J. Vac. Sci. Technol. A **14**, 535 (1996).
[37] C. Tian and C. R. Vidal, J. Phys. B **31**, 895 (1998).
[38] J. M. Tibbitt, R. Jensen, A. T. Bell, and M. Shen, Macromolecules **10**, 647 (1977).
[39] K.-H. Kochem, W. Sohn, K. Jung, H. Ehrhardt, and E. S. Chang, J. Phys. B **18**, 1253 (1985).
[40] K. M. Ervin, J. Ho, and W. C. Lineberger, J. Chem. Phys. **91**, 5974 (1989).
[41] V. G. Anicich, W. T. Huntress, Jr., and M. J. McEwan, J. Phys. Chem. **90**, 2446 (1986).
[42] J. S. Knight, C. G. Freeman, M. J. McEwan, V. G. Anicich, and W. T. Huntress, Jr., J. Phys. Chem. **91**, 3898 (1987).
[43] A. P. Hickman, J. Chem. Phys. **70**, 4872 (1979).
[44] M. Masi, C. Cavallotti, and S. Carra, Chem. Eng. Sci. **53**, 3875 (1998).
[45] J. Appel, H. Bockhorn, and M. Frenklach, Combust. Flame **121**, 122 (2000).
[46] L. E. Kline, W. D. Partlow, and W. E. Bies, J. Appl. Phys. **65**, 70 (1989).
[47] K. Bera, B. Farouk, and Y. H. Lee, Plasma Sources Sci. Technol. **10**, 211 (2001).
[48] J. A. Miller and C. T. Bowman, Prog. Energy Combust. Sci. **15**, 287 (1989).
[49] J. Perrin, O. Leroy, and M. C. Bordage, Contrib. Plasma Phys. **36**, 3 (1996).
[50] C. J. F. Böttcher and P. Borderwijk, *Theory of Electric Polarization* (Elsevier, Amsterdam, 1978).
[51] A. Chutjian, A. Garscadden, and J. M. Wadehra, Phys. Rep. **264**, 393 (1996).
[52] I. Platzner and P. Marcus, Int. J. Mass Spectrom. Ion Phys. **41**, 241 (1982).
[53] M. Frenklach, Phys. Chem. Chem. Phys. **4**, 2028 (2002).
[54] M. Frenklach and E. Feigelson, in *From Stardust to Planetesimals*, edited by Y. J. Pendelton and A. G. G. M. Tielens, Astron. Soc. Pacific Conf. Series Vol. 122 (Astronomical Society of the Pacific, San Francisco, 1997), p. 107.
[55] E. W. McDaniel and E. A. Mason, *The Mobility and Diffusion of Ions in Gases* (John Wiley & Sons, New York, 1973).
[56] R. A. Svehla, NASA Technical Report No. R 132, 1962 (unpublished).
[57] A. von Keudell, C. Hopf, T. Schwarz-Selinger, and W. Jacob, Nucl. Fusion **39**, 1451 (1999).
[58] H. Kojima, H. Toyada, and H. Sugai, Appl. Phys. Lett. **55**, 1292 (1989).
[59] C. Hopf, K. Letourneur, W. Jacob, T. Schwarz-Selinger, and A. von Keudell, Appl. Phys. Lett. **74**, 3800 (1999).
[60] E. Kovacevic and J. Winter (private communication).
[61] Ch. Deschenaux, Ph.D. thesis, Centre de Recherches en Physique des Plasmas, Association Euratom, Switzerland, 2002 (unpublished).
[62] O. Stepanovic, J. Berndt, and J. Winter, in *XXVIIth ICPIG Conference Proceedings*, The Netherlands, 2005 (unpublished).